LETTER

Massive Dirac fermions in a ferromagnetic kagome metal

Linda Ye[1]*, Mingu Kang[1]*, Junwei Liu[1]†, Felix von Cube[2]†, Christina R. Wicker[1], Takehito Suzuki[1], Chris Jozwiak[3], Aaron Bostwick[3], Eli Rotenberg[3], David C. Bell[2,4], Liang Fu[1], Riccardo Comin[1] & Joseph G. Checkelsky[1]

The kagome lattice is a two-dimensional network of corner-sharing triangles[1] that is known to host exotic quantum magnetic states[2–4]. Theoretical work has predicted that kagome lattices may also host Dirac electronic states[5] that could lead to topological[6] and Chern[7] insulating phases, but these states have so far not been detected in experiments. Here we study the d-electron kagome metal Fe_3Sn_2, which is designed to support bulk massive Dirac fermions in the presence of ferromagnetic order. We observe a temperature-independent intrinsic anomalous Hall conductivity that persists above room temperature, which is suggestive of prominent Berry curvature from the time-reversal-symmetry-breaking electronic bands of the kagome plane. Using angle-resolved photoemission spectroscopy, we observe a pair of quasi-two-dimensional Dirac cones near the Fermi level with a mass gap of 30 millielectronvolts, which correspond to massive Dirac fermions that generate Berry-curvature-induced Hall conductivity. We show that this behaviour is a consequence of the underlying symmetry properties of the bilayer kagome lattice in the ferromagnetic state and the atomic spin–orbit coupling. This work provides evidence for a ferromagnetic kagome metal and an example of emergent topological electronic properties in a correlated electron system. Our results provide insight into the recent discoveries of exotic electronic behaviour in kagome-lattice antiferromagnets[8–10] and may enable lattice-model realizations of fractional topological quantum states[11,12].

The kagome lattice (Fig. 1a) is a network with trihexagonal $(3.6)^2$ Archimedes tiling that has been studied extensively in the context of frustration-induced quantum-spin-liquid phases[2–4]. In terms of electronic structure, simple tight-binding models on kagome lattices have long been known to yield unusual features, including dispersionless bands and Dirac points (Fig. 1b); the Dirac points appear in a manner similar to those in hexagonal graphene lattices[13]. Although such features have not previously been observed in experiments, theoretical interest has persisted and lead to several further predictions. Of particular interest are kagome networks in which time reversal symmetry is broken via ferromagnetism (Fig. 1c)[5,7,11], which has the effect of splitting the spin-degenerate Dirac bands (Fig. 1d). Further inclusion of spin–orbit coupling (Fig. 1e) yields various gapped phases (Fig. 1f) with integer[7] or fractional[11,12] topological invariants (Chern numbers). When the chemical potential is within the Dirac gap, the intrinsic anomalous Hall effect, which results from the integration of Berry curvature over the Brillouin zone, is quantized and in principle affords detection of the Chern number of the wavefunction of the system[14,15]. More generally, with multiple bands and arbitrary positions of the chemical potential, such measurements can detect the Berry curvature that is concentrated by massive Dirac bands[16].

Despite a broad theoretical understanding of electronic Berry-phase effects in ferromagnetic kagome models and extensive studies of kagome insulators[4], experimental realization of the former has been challenging, in part owing to the relative rarity of kagome materials. An approach to realizing metallic kagome networks in the hexagonal transition-metal stannides A_xSn_y (A = Mn, Fe or Co; $x{:}y$ = 3:1, 3:2 or 1:1) has been reported[17]. As shown in Fig. 1g for A = Fe (studied here), starting from a single layer of a hexagonal close-packed structure of iron atoms, a kagome net emerges naturally by replacing a 2×2 sub-lattice (dashed cell) with tin atoms, resulting in an Fe_3Sn plane with an underlying iron kagome lattice.

Here we study the bilayer kagome compound Fe_3Sn_2 (space group $R\bar{3}m$; hexagonal lattice constants $a = 5.338$ Å and $c = 19.789$ Å)—a structural variation of Fe_xSn_y that includes a stanene layer sandwiched between Fe_3Sn bilayers (Fig. 1h). In Fig. 1h we also show a corresponding transmission electron microscopy image of a $(10\bar{1}0)$ cross-section of a single crystal of Fe_3Sn_2, which reveals the Fe_3Sn and stanene layers. Previous studies[17] have identified Fe_3Sn_2 as an unusual magnetic conductor with a high Curie temperature of $T_C = 670$ K. Although attention was originally focused on the zero-field spin structure[18], recent studies have focused on the formation of skyrmion bubbles[19] and a substantial anomalous Hall effect[20,21] at finite field. The latter is particularly interesting in comparison with the structurally related antiferromagnets Mn_3Sn and Mn_3Ge, which were recently reported to have a large room-temperature anomalous Hall response[8,9] and possible Weyl fermion states[10].

Measurements of magnetization M as a function of magnetic induction B along the c axis (Fig. 2a) demonstrate that the system is a soft ferromagnet, with the saturation field and saturation magnetization M_s depending mildly on temperature T. The saturation magnetization M_s reaches approximately $1.9\mu_B$ per iron atom at low temperature T (where μ_B is the Bohr magneton; Fig. 2a, inset). The crystals exhibit high metallicity, with the residual resistivity ratio of $\rho(300\,\text{K})/\rho(2\,\text{K}) \approx 25$ (Extended Data Fig. 1) allowing characterization by electrical transport. The transverse resistivity in the kagome plane $\rho_{yx}(B)$ (Fig. 2b) strongly reflects $M(B)$—a characteristic of the anomalous Hall effect[20,21]. In ferromagnetic conductors it is conventional[16] to express $\rho_{yx}(B)$ in terms of contributions from the ordinary (Lorentz-force) Hall coefficient R_0 and the anomalous Hall coefficient R_s: $\rho_{yx} = R_0B + R_sM$; as shown in the inset of Fig. 2b, R_0 depends mildly on T (corresponding to 6×10^{21} electrons per cm^3 at low T), whereas R_s is much larger but decreases with decreasing T.

To elucidate the role of the bilayer kagome lattice further, we examine the associated Hall conductivities in the kagome plane. The contributions to the total Hall conductivity $\sigma_{xy} = \sigma_{xy}^N + \sigma_{xy}^A$, where the superscript 'N' ('A') denotes the normal (anomalous) component, can be separated by using the field linearity of σ_{xy}^N in the low-Hall-angle limit (Methods). Although σ_{xy}^A is known to have contributions of both intrinsic (Berry curvature) and extrinsic (scattering) origin[16], it has recently
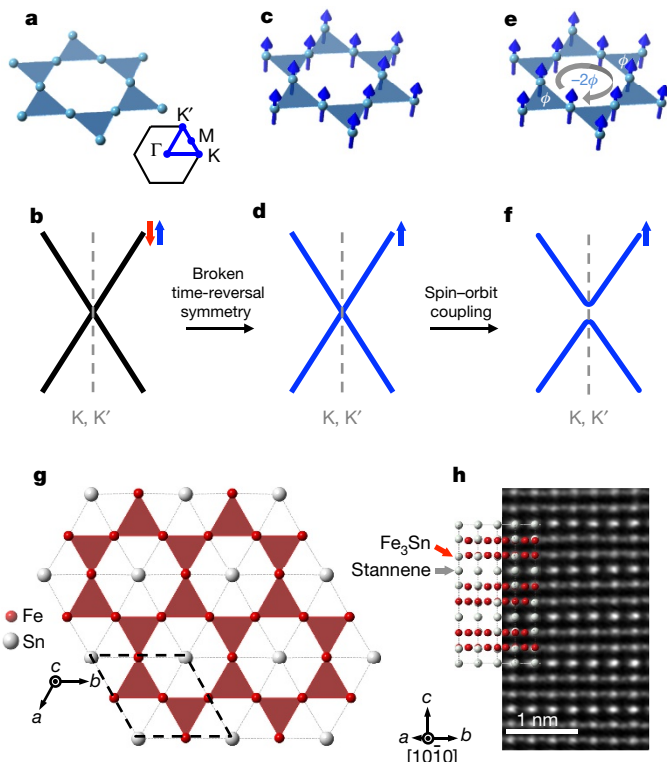

Figure 1 | The kagome structure and Fe₃Sn₂. a, b, Structure of the kagome lattice (**a**) and the associated Dirac point in the nearest-neighbour tight-binding model (**b**), with the Brillouin zone shown in the inset. The band is degenerate, as denoted with red and blue spins. **c, d,** Ferromagnetic kagome lattice with broken time-reversal symmetry (moments in blue) (**c**) and the associated spin-polarized Dirac band with coupling between the magnetization and spin (**d**). **e, f,** Spin–orbit-coupled ferromagnetic kagome lattice with Berry phase ϕ accrued via hopping (**e**) and the corresponding gapped Dirac spectrum (**f**). **g,** The Fe₃Sn kagome plane in Fe₃Sn₂, with the kagome network shown in red. **h,** Transmission electron microscopy cross-section of Fe₃Sn₂ and the corresponding Fe₃Sn and stanene layers viewed from the [10$\bar{1}$0] direction.

been demonstrated that the insensitivity of the latter to thermal excitations allows the parameterization $\sigma^{A}_{xy} = f(\sigma_{xx,0})\sigma^{2}_{xx} + \sigma^{int}_{xy}$, where $f(\sigma_{xx,0})$ is a function of the residual conductivity $\sigma_{xx,0}$, σ_{xx} is the conductivity and σ^{int}_{xy} is the intrinsic anomalous Hall conductivity[22]. Because σ^{int}_{xy} does not depend on the scattering rate, in a system with substantial Berry curvature, σ^{int}_{xy} is then the remnant σ^{A}_{xy} that is observed as $\sigma^{2}_{xx} \rightarrow 0$ (Fig. 2c, top inset). Figure 2c demonstrates that $\sigma^{A}_{xy}(T)$ remains relatively unchanged from this remnant value at high temperature, until $T \approx 100$ K at which an upturn concomitant with increasing $\sigma_{xx}(T)$ is observed. This upturn is indicative of the onset of an extrinsic response, which is expected[16] with the longer relaxation time in this range of σ_{xx}; the subsequent σ^{2}_{xx} scaling of the additional σ^{A}_{xy} (Fig. 2c, top inset) is also consistent with an extrinsic origin[22,23]. The scattering-rate-independent value of σ^{A}_{xy} at high T persists, varying by about 10% down to $T = 2$ K (158 ± 16 Ω^{-1} cm^{-1}), which corresponds to approximately $0.27e^{2}/h$ per kagome bilayer, where e is the electronic charge and h is the Planck constant. We identify this contribution as σ^{int}_{xy} (Fig. 2c), with behaviour akin to that expected from a massive Dirac band[23].

These observations point to a substantial Berry-curvature contribution to the transport response in Fe₃Sn₂ in a geometry that samples the kagome planes (Fig. 2c, middle inset). We also measured the Hall response perpendicular to the kagome plane σ_{zx} (Fig. 2c, lower inset). This out-of-plane signal is much smaller (Fig. 2c), with the ratio $|\sigma^{A}_{zx}/\sigma^{A}_{xy}|$ being less than 10% at the highest T, indicating a large relative enhancement of the Berry curvature in the kagome plane.

To examine the origin of this Hall response further, we measured the electronic structure of Fe₃Sn₂ by using angle-resolved photoemission spectroscopy (ARPES). In Fig. 3a, b we show the experimental Fermi surface and energy–momentum dispersion, respectively, of the electronic bands along high-symmetry directions parallel to the kagome planes, measured at $T = 20$ K (see also Extended Data Fig. 2). A rich spectrum of electronic excitations with hexagonal symmetry is observed, consistent with the metallicity and crystallographic structure described above. More notably, linearly dispersing Dirac cones are observed at the corner points K and K′ of the Brillouin zone. This spectrum, which is reminiscent of the electronic structure of graphene[24], is the long-sought realization of kagome-derived Dirac fermions[5]. These Dirac-like bands are shown in detail in the high-resolution energy–momentum section of the ARPES data across the K point in Fig. 3c (data are collected along the blue dashed line in Fig. 3a and then symmetrized in momentum about K); two Dirac cones, separated in energy but centred at K, are resolved. Hereafter, we focus on these bands and their role in generating Berry curvature.

The two-fold Dirac cones can also be identified in constant-energy contours (Fig. 3d). At the Fermi energy E_F (Fig. 3d, top layer), a pair of Dirac cones forms two electron pockets centred at K: a circular inner pocket and a trigonally warped outer pocket. Moving down from E_F each pocket shrinks, forming apparent Dirac points at binding energies of 70 meV (Fig. 3d, second layer) and 180 meV (Fig. 3d, bottom layer). At the midpoint energy (125 meV), the two Dirac cones cross and, within our experimental resolution, form a ring of Dirac points in the x–y momentum plane. The experimental electronic structure near the K point is therefore characterized by two energy-split ($\Delta E = 110$ meV) interpenetrating Dirac cones. This splitting is a natural consequence of the bilayer kagome structure, similarly to the case of multilayer graphene[24], whereas the exchange splitting due to magnetic order is expected[25] to be much larger (in excess of 2 eV). Photon-energy-dependent ARPES (Extended Data Fig. 4) reveals negligible variation in the Dirac bands as a function of out-of-plane momentum k_z, indicating quasi-two-dimensional (quasi-2D) bands confined to the iron kagome bilayer.

Having established the Dirac fermiology of Fe₃Sn₂, we focus on the role of spin–orbit coupling and the possible mass acquisition of the Dirac bands. Inspection of the raw ARPES data reveals that the spectral intensity at the Dirac point is suppressed substantially (Extended Data Fig. 3d), which is more clearly visualized in the second derivative of the ARPES map (Fig. 3e). Analysis of the energy distribution curves displayed in Fig. 3f reveals a break between the upper and lower branches of the Dirac cone, which signals the opening of an energy gap Δ. A quantitative analysis performed by fitting the energy distribution curves with Gaussian peaks returns $\Delta = 30 \pm 5$ meV (Methods). This value is similar to that predicted previously for spin–orbit-coupled 3d transition metals in kagome lattices[7], but smaller than that observed in magnetically doped topological insulators (about 50 meV)[26,27] and in hydrogen-decorated graphene (at least 0.5 eV)[28].

The emergence of massive Dirac fermions in Fe₃Sn₂ can be understood as a combination of ferromagnetic splitting and spin–orbit coupling in the underlying kagome geometry. Motivated by the weak k_z dispersion observed in ARPES, we consider a stacked system of kagome layers. In Fig. 4a we show a perfect Fe₃Sn kagome layer and the corresponding Brillouin zone. The kagome layer has two-fold and three-fold rotational symmetries (C_{2x} and C_{3z}, respectively) that leave the K and K′ points invariant and thus form point group D_3. In the absence of spin–orbit coupling, the two-fold-degenerate crossing (Dirac) points at K and K′ belong to a two-fold irreducible representation (E) and are therefore protected. As illustrated in Fig. 4b, a Dirac crossing can be observed at K in a tight-binding model H_K for nearest-neighbour hopping on the kagome sites:
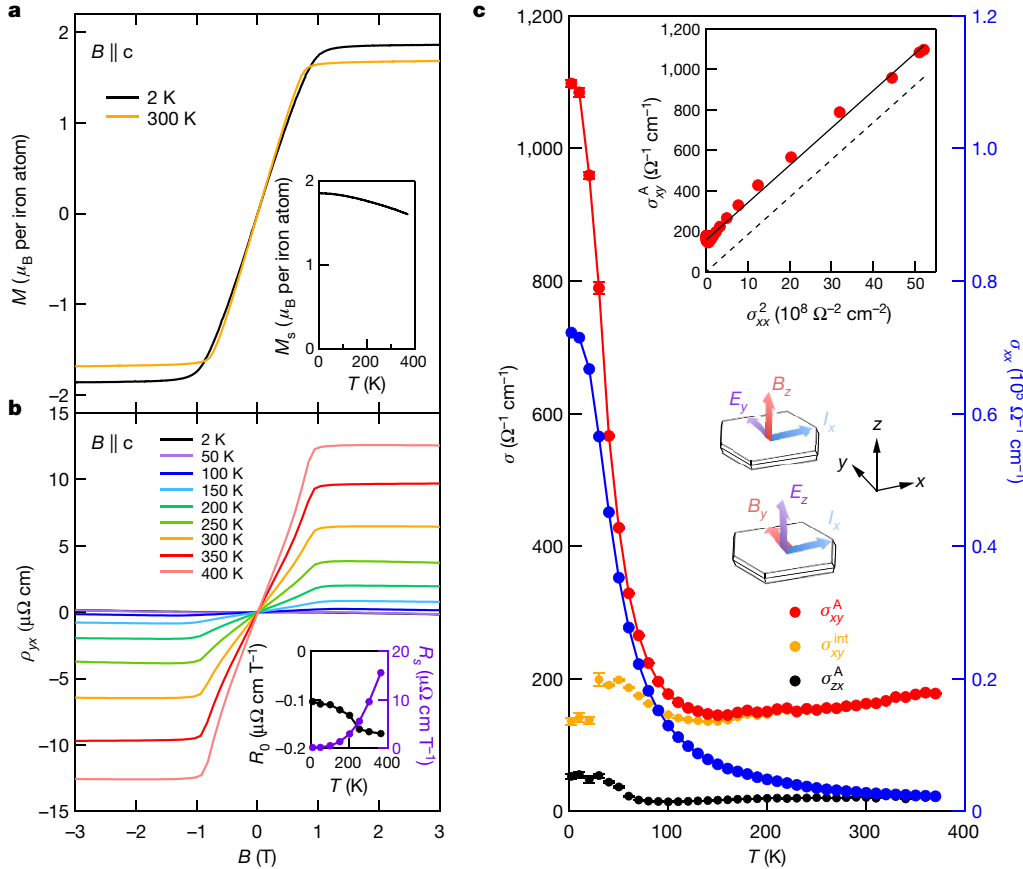
$$H_K = \sum_{\langle ij \rangle} t c_i^{\dagger} c_j \tag{1}$$

Figure 2 | Anomalous Hall response of Fe₃Sn₂. a, Magnetization M of Fe₃Sn₂ along the c axis as a function of magnetic induction B at room temperature ($T = 300$ K; orange) and low temperature ($T = 2$ K; black). The inset shows the saturation magnetization M_s (measured at 2 T) as a function of temperature T. **b**, Hall resistivity ρ_{yx} as a function of B. The inset shows the ordinary and anomalous Hall coefficients R_0 (black) and R_s (purple), respectively, as a function of T. **c**, Anomalous Hall conductivities σ_{xy}^A (red, left axis) and σ_{zx}^A (black, left axis) in the x–y and z–x planes, respectively, along with the longitudinal conductivity σ_{xx} (blue, right axis) and estimated intrinsic Hall conductivity σ_{xy}^{int} (orange, left axis). The measurement configurations for σ_{xy} (top) and σ_{zx} (bottom) are shown in the lower inset; I represents the charge current. The upper inset shows σ_{xy}^A plotted against σ_{xx}^2; the solid and dashed lines are the scaling curves (see text).

where $\langle ij \rangle$ indexes nearest-neighbour pairs, t is the hopping integral and c_j ($c_i^\dagger$) is the fermion annihilation (creation) operator, which is taken to be spin-polarized owing to exchange. The kagome bilayers in Fe₃Sn₂ (Fig. 4c) are tiled by triangles of two different bond lengths, 2.59 Å and 2.75 Å, as indicated by the red and blue shading. However, the combined unit of these kagome layers and the intervening stanene layer preserves the $\{C_{2x}, C_{3z}\}$ symmetry of the perfect kagome lattice and the Dirac points are thus protected by crystal symmetry in the absence of spin–orbit coupling. The additional layer degree of freedom further enriches the electronic structure. In particular, the ABA layer stacking of the structure in Fig. 4c gives rise to bonding–antibonding splitting[29], as seen in a simple tight-binding model with this additional hopping (Fig. 4d).

We next introduce Kane–Mele-type spin–orbit coupling H_{SOI} to the tight-binding model H_K, with

$$H_{SOI} = i \sum_{\langle ij \rangle} \lambda_{ij} (c_{i\uparrow}^\dagger c_{j\uparrow} - c_{i\downarrow}^\dagger c_{j\downarrow}) \qquad (2)$$

where λ_{ij} represents the effect of spin–orbit coupling and ↑ and ↓ denote the spin quantum number[30]. Writing $\lambda_{ij} = \lambda(\mathbf{E}_{ij} \times \mathbf{R}_{ij}) \cdot \mathbf{s}$, where λ is the spin–orbit coupling constant, $\mathbf{E}$ is the electric field on the hopping path, $\mathbf{R}$ is the hopping vector and $\mathbf{s}$ represents the electron spin, for spin-polarized bands near K and K′ with non-zero z polarization s_z, H_{SOI} effectively reduces to the Haldane term[31]. Accordingly, for the single-layer case (Fig. 4b), when E_F is positioned in the Dirac gap, the system enters a Chern insulating phase with quantized anomalous Hall conductance[7,31].

To connect with the Hall response, we construct a $\mathbf{k} \cdot \mathbf{p}$ Hamiltonian near K and K′ for the dual Dirac fermions and fit to the ARPES data (Fig. 4e, inset; Methods). We then calculate the contribution of the massive Dirac bands to the Hall response by integrating the Berry curvature of the filled states, which yields $\sigma_{xy}^{calc} = (0.31 \pm 0.05)e^2/h$ at E_F for a kagome bilayer (Fig. 4e), comparable to the observed value of $\sigma_{xy}^{int} = (0.27 \pm 0.03)e^2/h$ per bilayer. Remarkably, despite the simplicity of our model, the action of the quasi-2D massive Dirac fermions at K and K′ largely accounts for the observed Hall response with the crystal viewed as a parallel network of bilayer kagome planes. However, there are limitations; for example, for a 2D model there is no contribution to the out-of-plane Hall response. We suggest instead that this out-of-plane response originates from the three-dimensional (3D) network of tin atoms and the associated k_z-dispersive bands near Γ (Methods). The relative smallness of σ_{zx}^A is then consistent with a minor contribution of tin-atom-derived bands to the overall Berry curvature. More generally, the model evidences the role of the concentration of Berry curvature in the quasi-2D massive Dirac bands, which have small E_F comparable to the spin–orbit coupling strength[16]. The robustness of the Hall response observed here is comparable to that of the Hall response that is driven by chiral antiferromagnetic order in Mn₃Sn (ref. 8) and Mn₃Ge (ref. 9); however, instead of originating from 3D Weyl nodes[10], the Hall response observed here is driven by quasi-2D Dirac fermions in a ferromagnetic kagome network interleaved with stanene layers.

By combining electrical transport measurements, ARPES and theoretical analysis, this study provides a comprehensive proof of
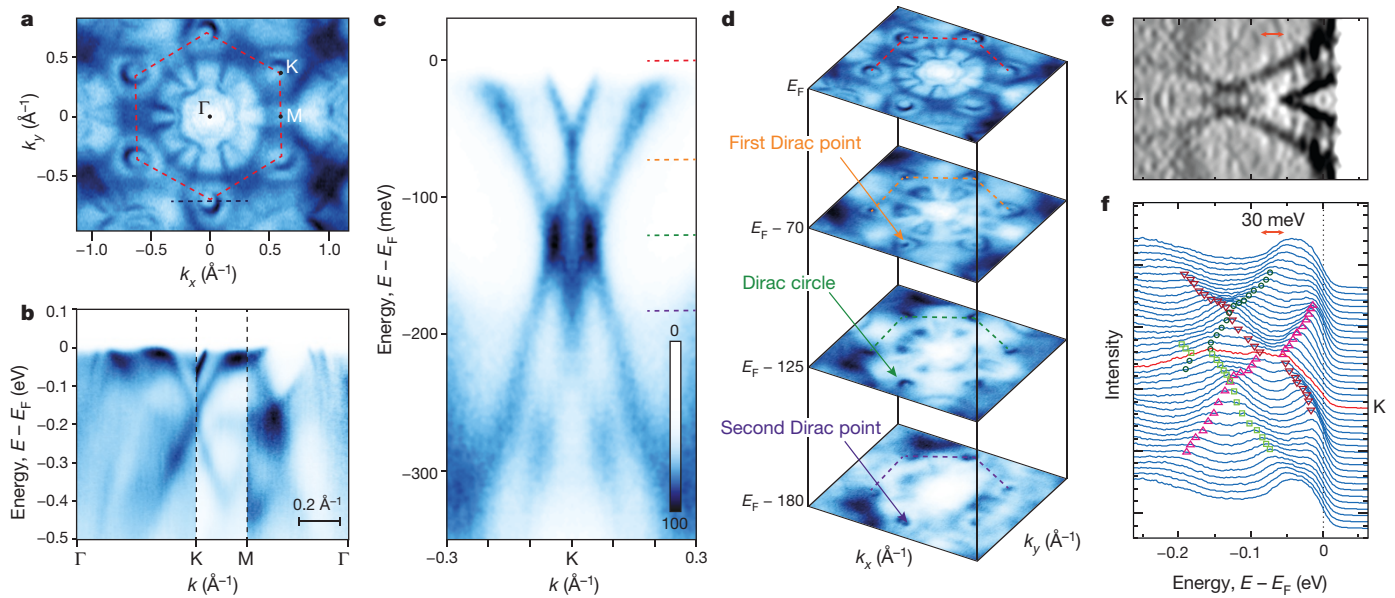
Figure 3 | Massive Dirac fermion at the zone corner of Fe₃Sn₂.
a, Experimentally obtained Fermi surface of Fe₃Sn₂. The hexagonal Brillouin zone (red dashed lines) and high-symmetry points (black dots) are marked. **b**, Experimentally determined band dispersion of Fe₃Sn₂ along the high-symmetry directions. **c**, High-resolution ARPES data, measured along the blue dashed line in **a** and then symmetrized with respect to K. The complete band dispersion is shown in Extended Data Fig. 3 (with a modified colour scale). **d**, Constant-energy maps at binding energies of 0 meV, 70 meV, 125 meV and 180 meV. Two electron pockets (top layer),

a first Dirac point (second layer), a Dirac circle (third layer) and a second Dirac point (bottom layer) can be clearly detected from the maps. The corresponding energies and Brillouin zone contours are marked with coloured dashed lines in **c** and **d**. **e**, **f**, The second-derivative plot (**e**) and the stack of energy distribution curves (**f**) across the Dirac points. Both panels share the momentum range and direction with **c**. The red double-headed arrow marks the discontinuity between the upper and lower branches of the Dirac cone. Coloured markers indicate the fitted band energies. All data were obtained using 92-eV photons.

principle for engineering band-structure singularities and topological phenomena in correlated systems. In particular, we realize lattice-driven[6,7,30,31] topological 3d electronic bands, which we suggest exhibit the defining properties of a ferromagnetic kagome metal. Viewed in isolation, the bands near K can be considered to exhibit

a 2D 'Chern gap'—a time-reversal-symmetry-broken topologically non-trivial phase that is intrinsic to stoichiometric materials and has a dominant contribution to the electrical response at temperatures of up to 300 K and above. To isolate these bands, as a step towards realizing high-temperature dissipationless modes[15], we propose finding
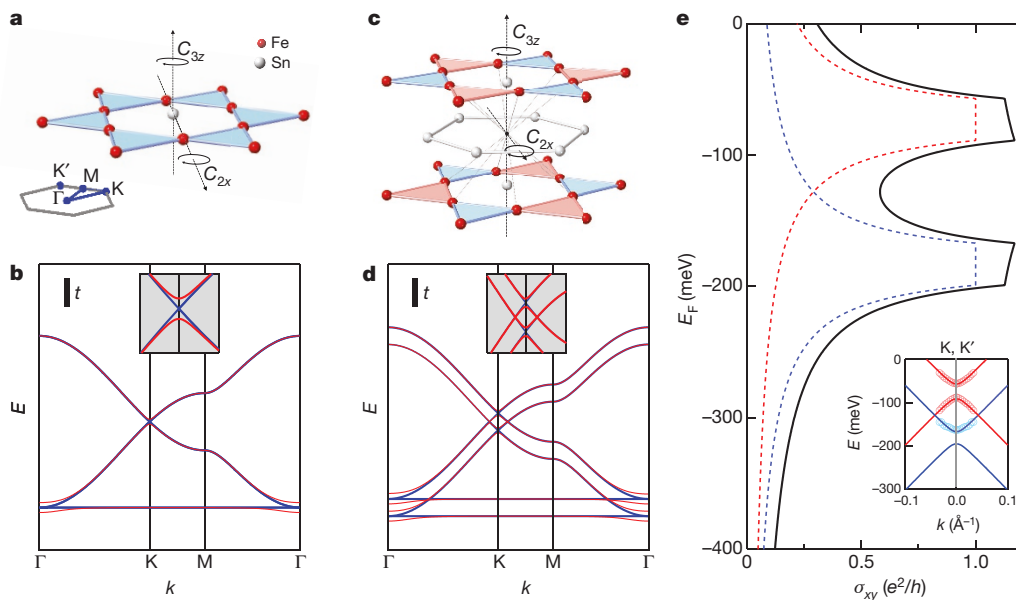

Figure 4 | Tight binding and hall conductivity of a kagome bilayer.
a, Two-fold (C₂ₓ) and three-fold (C₃ᵤ) rotation-axis symmetry operations of a single Fe₃Sn kagome layer. **b**, Tight-binding band model of the single-layer kagome lattice with (red) and without (blue) spin–orbit coupling. The inset shows a magnified view of the (avoided) crossing near K. **c**, C₂ₓ and C₃ᵤ symmetries of the 'breathing' kagome (illustrated by the red and blue inequivalent bonds) and stanene layers. **d**, Tight-binding band model of the double-layer kagome lattice with in-plane hopping t and inter-plane

hopping 0.3t, with (red) and without (blue) spin–orbit coupling. The inset shows a magnified view of the double Dirac structure near K. The spin–orbit coupling strength λ = 0.05t for **b** and **d**. **e**, Anomalous Hall conductivity σ_{xy} as a function of Fermi energy E_F from the **k** · **p** model (black solid curve; see text). The red and blue dashed curves represent the contributions from the upper and lower Dirac bands, respectively. The inset shows the fit (solid lines) of a massive Dirac dispersion to the ARPES results (circles) near K.

simplified structures with a single kagome layer per unit cell or pursuing 2D morphologies via thin films or exfoliation of related materials with van der Waals bonding. Furthermore, the frustrated hopping network of kagome lattices is predicted to support electronic bands (as in Fig. 4d) with non-zero Chern number and enhanced electronic correlation[5]. Searching for these bands by chemically doping Fe_3Sn_2, by using alternative structures and stoichiometries in A_xSn_y or by using other spin–orbit-coupled 4*d* and 5*d* kagome metals are key to realizing new, magnetically driven fractionalized phases of matter[11,12].

1. O'Keeffe, M. & Hyde, B. G. *Crystal Structures. I. Patterns and Symmetry* Ch. 5 (Mineralogical Society of America, 1996).
2. Sachdev, S. Kagome- and triangular-lattice Heisenberg antiferromagnets: ordering from quantum fluctuations and quantum-disordered ground states with unconfined bosonic spinons. *Phys. Rev. B* **45**, 12377–12396 (1992).
3. Han, T.-H. *et al.* Fractionalized excitations in the spin-liquid state of a kagome-lattice antiferromagnet. *Nature* **492**, 406–410 (2012).
4. Zhou, Y., Kanoda, K. & Ng, T.-K. Quantum spin liquid states. *Rev. Mod. Phys.* **89**, 025003 (2017).
5. Mazin, I. I. *et al.* Theoretical prediction of a strongly correlated Dirac metal. *Nat. Commun.* **5**, 4261 (2014).
6. Guo, H.-M. & Franz, M. Topological insulator on the kagome lattice. *Phys. Rev. B* **80**, 113102 (2009).
7. Xu, G., Lian, B. & Zhang, S.-C. Intrinsic quantum anomalous Hall effect in the kagome lattice $Cs_2LiMn_3F_{12}$. *Phys. Rev. Lett.* **115**, 186802 (2015).
8. Nakatsuji, S., Kiyohara, N. & Higo, T. Large anomalous Hall effect in a non-collinear antiferromagnet at room temperature. *Nature* **527**, 212–215 (2015).
9. Nayak, A. K. *et al.* Large anomalous Hall effect driven by a nonvanishing Berry curvature in the noncolinear antiferromagnet Mn_3Ge. *Sci. Adv.* **2**, e1501870 (2016).
10. Kuroda, K. *et al.* Evidence for magnetic Weyl fermions in a correlated metal. *Nat. Mater.* **16**, 1090–1095 (2017).
11. Tang, E. & Wen, X.-G. High-temperature fractional quantum Hall states. *Phys. Rev. Lett.* **106**, 236802 (2011).
12. Bergholtz, E. J., Liu, Z., Trescher, M., Moessner, R. & Udagawa, M. Topology and interactions in a frustrated slab: tuning from Weyl semimetals to $C > 1$ fractional Chern insulators. *Phys. Rev. Lett.* **114**, 016806 (2015).
13. Wallace, P. R. The band theory of graphite. *Phys. Rev.* **71**, 622–634 (1947).
14. Thouless, D. J., Kohmoto, M., Nightingale, M. P. & den Nijs, M. Quantized Hall conductance in a two-dimensional periodic potential. *Phys. Rev. Lett.* **49**, 405–408 (1982).
15. Chang, C.-Z. *et al.* Experimental observation of the quantum anomalous Hall effect in a magnetic topological insulator. *Science* **340**, 167–170 (2013).
16. Nagaosa, N., Sinova, J., Onoda, S., MacDonald, A. H. & Ong, N. P. Anomalous Hall effect. *Rev. Mod. Phys.* **82**, 1539–1592 (2010).
17. Giefers, H. & Nicol, M. High pressure X-ray diffraction study of all FeSn intermetallic compounds and one FeSn solid solution. *J. Alloys Compd.* **422**, 132–144 (2006).
18. Le Caër, G., Malaman, B. & Roques, B. Mössbauer effect study of Fe_3Sn_2. *J. Phys. F* **8**, 323–336 (1978).
19. Hou, Z. *et al.* Observation of various and spontaneous magnetic Skyrmionic bubbles at room temperature in a frustrated kagome magnet with uniaxial magnetic anisotropy. *Adv. Mater.* **29**, 1701144 (2017).
20. Kida, T. *et al.* The giant anomalous Hall effect in the ferromagnet Fe_3Sn_2—a frustrated kagome metal. *J. Phys. Condens. Matter* **23**, 112205 (2011).
21. Wang, Q., Sun, S., Zhang, X., Pang, F. & Lei, H. Anomalous Hall effect in a ferromagnetic Fe_3Sn_2 single crystal with a geometrically frustrated Fe bilayer kagome lattice. *Phys. Rev. B* **94**, 075135 (2016).
22. Tian, Y., Ye, L. & Jin, X. Proper scaling of the anomalous Hall effect. *Phys. Rev. Lett.* **103**, 087206 (2009).
23. Shitade, A. & Nagaosa, N. Anomalous Hall effect in ferromagnetic metals: role of phonons at finite temperature. *J. Phys. Soc. Jpn* **81**, 083704 (2012).
24. Kim, K. S. *et al.* Coexisting massive and massless Dirac fermions in symmetry-broken bilayer graphene. *Nat. Mater.* **12**, 887–892 (2013).
25. Sales, B. C., Saparov, B., McGuire, M. A., Singh, D. J. & Parker, D. S. Ferromagnetism of Fe_3Sn and alloys. *Sci. Rep.* **4**, 7024 (2014).
26. Chen, Y. L. *et al.* Massive Dirac fermion on the surface of a magnetically doped topological insulator. *Science* **329**, 659–662 (2010).
27. Xu, S. Y. *et al.* Hedgehog spin texture and Berry's phase tuning in a magnetic topological insulator. *Nat. Phys.* **8**, 616–622 (2012).
28. Balog, R. *et al.* Bandgap opening in graphene induced by patterned hydrogen adsorption. *Nat. Mater.* **9**, 315–319 (2010).
29. Ishii, Y., Harima, H., Okamoto, Y., Yamaura, J. & Hiroi, Z. YCr_6Ge_6 as a candidate compound for a kagome metal. *J. Phys. Soc. Jpn* **82**, 023705 (2013).
30. Kane, C. L. & Mele, E. J. Quantum spin Hall effect in graphene. *Phys. Rev. Lett.* **95**, 226801 (2005).
31. Haldane, F. D. M. Model for a quantum Hall effect without Landau levels: condensed-matter realization of the "parity anomaly". *Phys. Rev. Lett.* **61**, 2015–2018 (1988).

METHODS

Single-crystal growth. Single crystals of Fe_3Sn_2 were grown using an I_2-catalysed reaction. A stoichiometric ratio of Fe and Sn powders was sealed in a quartz tube with approximately 1% I_2 by mass and kept in a horizontal three-zone furnace with a temperature gradient from 750 °C to 650 °C for five weeks followed by water quenching to stabilize the Fe_3Sn_2 phase. Hexagonal, plate-like crystals of sub-millimetre size (Extended Data Fig. 1a, inset) formed near the high-temperature region as has been reported previously[32] for Fe_3Ge. The hexagonal surfaces were confirmed as (0001) kagome planes by using single-crystal X-ray diffraction.

Magnetization measurements. Magnetization measurements were performed using a commercial superconducting quantum interference device (SQUID) magnetometer with the field oriented along the c axis and in the a–b plane. Demagnetization corrections were performed for all measurements. The measured saturation moment ($1.9\mu_B$ per Fe atom) is consistent with previous reports[18,19,33].

Transport measurements. Four probe transport measurements were performed for longitudinal and Hall resistivity in a commercial cryostat with a superconducting magnet. High-field transport measurements in fields of up to 31 T were performed in a He-3 cryostat at Cell-9 of the National High Magnetic Field Laboratory. For measurements in the kagome plane, the field was applied along the [0001] direction with current and voltages in the kagome plane. For Hall measurements perpendicular to the kagome plane, the magnetic field and current were applied orthogonally in the kagome plane and the out-of-plane voltage is measured. The choice of coordination for in-plane and out-of-plane Hall measurements is such that, for the ordinary Hall effect of holes, $\sigma_{xy} > 0$ when the field is applied along the $+z$ direction and $\sigma_{zx} > 0$ ($\sigma_{xz} < 0$) when the field is applied along the $+y$ direction. Electrical signals were detected using standard AC lock-in techniques with a typical current density of 10 A cm^{-2}. To correct for contact misalignment, the measured longitudinal and transverse voltages were field-symmetrized and field-antisymmetrized, respectively. Demagnetization corrections were performed for all measurements.

Scanning transmission electron microscopy (STEM). STEM experiments were conducted at a probe-corrected STEM (JEOL ARM) operated at an acceleration voltage of 200 kV. Fe_3Sn_2 samples were prepared by a Helios focused-ion beam (FEI), operated at an acceleration voltage of 30 kV for the gallium beam during lift-out and of 2 kV during polishing. Additional polishing was performed at 1 kV and 0.5 kV with a NanoMill (Fischione). At both acceleration voltages, samples were polished for 20 min on each side.

Angle-resolved photoemission spectroscopy (ARPES). ARPES experiments were conducted at the Microscopic and Electronic Structure Observatory (MAESTRO) at beamline 7 (main data) and at the meV Resolution Soft X-ray Inelastic Scattering Beamline (MERLIN) at beamline 4 (preliminary measurement) of the Advanced Light Source. The two ARPES endstations are equipped with R4000 hemispherical electron analysers (VG scienta, Sweden). Data in Fig. 3 and Extended Data Fig. 3 were collected at 20 K with a photon energy of 92 eV, which maximizes the ARPES spectral weight of the Dirac bands. The photon-energy-dependent measurement was conducted from 45 eV to 120 eV (Extended Data Fig. 4). Energy and momentum resolutions were better than 15 meV and 0.01 $Å^{-1}$, respectively. Fe_3Sn_2 samples were cleaved in the ultrahigh-vacuum chamber with a base pressure of better than 4×10^{-11} torr. All of the data were collected within 8 h after cleaving to minimize the effect of sample degradation. Six different samples from various growth batches were analysed to confirm the consistency of results.

Longitudinal electrical transport. The resistivity in the kagome plane of sample C1 as a function of temperature, $\rho(T)$, is shown in Extended Data Fig. 1a. A metallic response is seen at all T, with a residual resistivity ratio of $\rho(300\,K)/\rho(2\,K) = 25$. The magnetoresistance for magnetic induction B normal to and within the kagome plane is shown in Extended Data Fig. 1b, c, respectively. In both figures, the electrical current I is perpendicular to the applied field. For $B \parallel c$ (Extended Data Fig. 1b), we observe a non-monotonic response below the saturation field ($B \leq 1.2$ T), which may reflect a transition through a skyrmion bubble phase, as was reported recently[19]. This structure is absent for $B \perp c$ (Extended Data Fig. 1c). In addition, for both $B \parallel c$ and $B \perp c$, a negative linear magnetoresistance characteristic of magnon suppression[34] is observed at high T.

Analysis of the Hall effect. In a ferromagnetic metal, the total Hall conductivity is composed of contributions from the normal Hall effect ('N') induced by Lorentz force and the anomalous Hall effect ('A'): $\sigma_{xy} = \sigma_{xy}^N + \sigma_{xy}^A$. In the limit of small Hall angle ($\Theta_H \equiv \rho_{yx}/\rho_{xx} \ll 1$), we have $\sigma_{xy} \approx B/(ne\rho_{xx}^2)$, where n is the carrier density and e is the electronic charge. Given the relatively small magnetoresistance, we extract σ_{xy}^N from a linear fit of $\sigma_{xy}(B)$ for fields above saturation (1.7 T to 5 T), with the intercept returning σ_{xy}^A (Extended Data Fig. 2a). That the condition $\Theta_H \ll 1$ is satisfied is confirmed to high field, with $\Theta_H \ll 0.04$ for fields up to 30 T (Extended Data Fig. 2b).

We measured the anomalous Hall effect at temperature $T = 300$ K in multiple samples. We find a consistently enhanced anomalous Hall conductivity in the kagome plane σ_{xy}^A relative to out of the kagome plane σ_{zx}^A. For samples C1, C4 and C5, the observed value of σ_{xy}^A is $163.6\,\Omega^{-1}\,cm^{-1}$, $179.1\,\Omega^{-1}\,cm^{-1}$ and $138.8\,\Omega^{-1}\,cm^{-1}$, respectively. For samples C2, C4, C5 and C6, the observed value of σ_{zx}^A is $20.5\,\Omega^{-1}\,cm^{-1}$, $22.0\,\Omega^{-1}\,cm^{-1}$, $55.6\,\Omega^{-1}\,cm^{-1}$ and $53.7\,\Omega^{-1}\,cm^{-1}$, respectively. The T dependence for C1 and C4 is shown in Fig. 2.

Energy–momentum dispersion along high-symmetry directions. Extended Data Fig. 3a, e shows the experimental Fermi surface of Fe_3Sn_2 obtained from different orientations of the crystal axis with respect to the photoelectron emission plane. Extended Data Fig. 3b–d, f, g shows the experimental band dispersion of Fe_3Sn_2 along high-symmetry directions. Despite the occurrence of a complex-matrix-elements effect near the K point, the structure of the two interpenetrating Dirac cones is clearly visible in all momentum directions probed in this experiment. In Extended Data Fig. 3h, energy distribution curves at different Brillouin-zone corner points are shown. All energy distribution curves show a consistent two-peak structure near the first Dirac point, signalling a gap opening. The velocity of the Dirac fermions v_D is found to be isotropic in the kagome plane, with magnitude $v_D = (1.76 \pm 0.11) \times 10^5\,m\,s^{-1}$, comparable to that observed recently in iron pnictide[35] and selenide[36] superconductors, but lower than in graphene[37,38], possibly reflecting the correlated character of the Fe-3d states.

Photon-energy-dependent ARPES. Photon-energy-dependent ARPES probes the variation of the band structure along the momentum direction perpendicular to the sample surface (the k_z direction in our geometry)[39]. The experiment here was conducted by varying the photon energy from 55 eV to 120 eV. The ARPES spectral weight of the localized d electrons is suppressed at low photon energy, so we report only the results from 90 eV to 120 eV. Considering the large c-axis lattice constant ($c = 19.8$ Å), the photon energy range presented here spans more than three complete Brillouin zones. The dependence on photon energy varies substantially between different bands. For example, the dispersion of the innermost electron pocket at Γ (Extended Data Fig. 4b) depends critically on the photon energy (k_z), whereas the dispersion of Dirac bands shows negligible dependence on k_z. The latter finding demonstrates the pronounced 2D nature of the Dirac fermions that we observed. We ascribe the highly dispersive bands centred at Γ to the 3D network of Sn atoms within the crystal structure.

Tight-binding models. We use a simple 2D tight-binding model to capture the symmetry-protected Dirac nodes at K and K′ in the single-layer (Fig. 4a) and bilayer (Fig. 4c) kagome lattice. Starting with the former, in the absence of spin–orbit coupling, the nearest-neighbour tight-binding model H_K (equation (1)) yields Dirac bands and a dispersionless band (Fig. 4b). For the bilayer kagome lattice, we include additional hopping $t_0 = 0.3t$ between the vertically displaced sites on each kagome layer, which introduces a layer splitting of the Dirac states in energy (Fig. 4d)[29]. We examine the effect of the spin–orbit interaction by adding a Kane–Mele-type term[30] H_{SOI} (equation (2)) in the leading-order nearest-neighbour hopping to the tight-binding model H_K with strength given by $\lambda(\boldsymbol{E}_{ij} \times \boldsymbol{R}_{ij}) \cdot \boldsymbol{s}$. The magnetic moments in Fe_3Sn_2 have been proposed to be subjected to spin reorientation and microscopic domain formation[19,33]; contributions to λ_{ij} arise from orthogonality of the hopping path and local electric-field and spin directions in each domain. In the simplified hopping model, these contributions are represented by an in-plane electric field and s_z, with $\lambda_{ij} = 0.05t$ in Fig. 4b, d. Similar Hamiltonians[40,41] have been used in the spin sector for insulating materials with kagome structures[40–43].

Model calculation of Hall conductivity. To connect with the Hall response, we first construct a $\boldsymbol{k} \cdot \boldsymbol{p}$ Hamiltonian near K and K′ for the dual Dirac fermions observed in the ARPES spectra:

$$H_D = [\hbar v_F(k_x\sigma_y - k_y\sigma_x)] \otimes I + E_0\tau_x + m\sigma_z \qquad (3)$$

where σ_i ($i = x, y, z$) are the Pauli matrices of pseudospin for each Dirac band, E_0 is the energy splitting of the Dirac bands described by the Pauli matrix τ_x, and $m = \Delta/2$ is the Dirac mass. To obtain the band parameters, we fit the observed dispersion $E(k)$ to the massive Dirac model $E_\pm^i(k) = \pm\sqrt{(\hbar v_D)^2 + (\Delta/2)^2} + E_0^i$, where E_0^i is the energy offset of the upper ($i = 1$) and lower ($i = 2$) Dirac bands from E_F. As shown in the inset of Fig. 4e, a satisfactory fit is found with $v_D = (1.85 \pm 0.15) \times 10^5\,m\,s^{-1}$, $\Delta = 32 \pm 3$ meV, $E_0^1 = -73 \pm 5$ meV and $E_0^2 = -182 \pm 5$ meV. The Dirac band centred at 73 meV can be analysed reliably, whereas matrix-element effects and the proximity of neighbouring bands interfere with the intensity distribution of the lower Dirac point. Applying the same set of Fermi velocity and mass for the upper and lower Dirac bands, we then calculate the contribution of the massive Dirac bands to the Hall response by integrating the Berry curvature over the filled states described by equation (3) as follows.

The Hall conductivity σ_{xy} can be considered a geometric quantity that characterizes the mapping from the k_x–k_y momentum plane to the two-component

Dirac band structure[44]. For a general two-level Hamiltonian $\mathbf{d}(\mathbf{k}) \cdot \boldsymbol{\sigma}$, (where $\boldsymbol{\sigma} = \{\sigma_x, \sigma_y, \sigma_z\}$ and $\mathbf{d}(\mathbf{k})$ is a generic vector), the wave functions may be represented as points on the unit Bloch sphere by $\pm\hat{\mathbf{d}}(\mathbf{k}) = \mathbf{d}(\mathbf{k})/|\mathbf{d}(\mathbf{k})|$, where the $\pm$ denotes the two eigenstates of the Hamiltonian at a given $\mathbf{k}$. σ_{xy} then takes the form[44]

$$\sigma_{xy} = \frac{e^2}{h} \iint_{\text{filled states}} \hat{\mathbf{d}} \cdot (\partial_x \hat{\mathbf{d}} \times \partial_y \hat{\mathbf{d}}) \mathrm{d}k_x \mathrm{d}k_y \qquad (4)$$

where the integrand (the Berry curvature) can be seen as the Jacobian associated with mapping the k_x–k_y plane to the unit sphere. Therefore, σ_{xy} is proportional to the total area covered on the unit sphere by the filled states. Also, because the integrand in equation (4) is a pseudoscalar, the states represented by $\pm\hat{\mathbf{d}}$ have opposite contributions to σ_{xy}.

The above formulation for σ_{xy} of a single Dirac fermion is illustrated in Extended Data Fig. 5 for the gapless and gapped cases. For the former (Extended Data Fig. 5a), the wavefunction of the Dirac fermions is confined to the equator of the Bloch sphere and therefore $\sigma_{xy} = 0$. Extended Data Fig. 5b shows the case in which the lower branch of the massive Dirac cone is filled. In this case, the occupied states span the lower hemisphere and yield $\sigma_{xy} = 0.5e^2/h$. When the upper branch of the gapped Dirac fermion is partially filled (Extended Data Fig. 5c), a contribution of opposite sign appears. The resulting σ_{xy} for a single Dirac fermion is therefore

$$\sigma_{xy} = \begin{cases} \dfrac{e^2}{h} \dfrac{S}{4\pi} & \text{for } S \leq 2\pi \\[2ex] \dfrac{e^2}{h} \dfrac{4\pi - S}{4\pi} & \text{for } S \geq 2\pi \end{cases}$$

where S is the total area of the filled states on the Bloch sphere; this is shown in Extended Data Fig. 5d as a function of energy E normalized by $h\nu_F$ (where ν_F is the Fermi velocity).

The above formulation is consistent with that expected from the semi-classical Boltzmann equation and Kubo formalism for a single massive Dirac fermion[45]:

$$\sigma_{xy} = \frac{e^2}{h} \frac{\Delta/2}{\sqrt{(\Delta/2)^2 + (\hbar\nu_F k_F)^2}} \qquad (5)$$

where Δ is the size of the Dirac gap and k_F is the Fermi wavevector. From equation (5) and Extended Data Fig. 5c, we see that σ_{xy} is maximized to $e^2/(2h)$ when E_F is within the gap and drops outside the gap with a long tail[46,47]. Importantly, the massive Dirac fermions at the K and K′ valleys are related by inversion symmetry and therefore contribute similarly to the Berry curvature; the contribution from equation (5) is therefore doubled. With the experimental fits to

equation (3) and adding up the contributions from the upper and lower Dirac points to the anomalous Hall conductivity described by equations (4) and (5), we obtain the energy-dependent 2D Hall conductance σ_{xy}^A (Fig. 4e). The Hall conductivity at the Fermi level evaluates to $\sigma_{xy}(E_F) = (0.31 \pm 0.05)e^2/h$. The uncertainty within this model arises from fitting the experimental band parameters near K; developing models that use the complete electronic structure and Berry curvature to compare to the experimental results is an important future direction.

Data availability. The data that support the findings of this study are available from the corresponding authors on reasonable request.

32. Drijver, J. W., Sinnema, S. G. & van der Woude, F. Magnetic properties of hexagonal and cubic Fe$_3$Ge. *J. Phys. F* **6,** 2165–2177 (1976).
33. Fenner, L. A., Dee, A. A. & Wills, A. S. Non-collinearity and spin frustration in the itinerant kagome ferromagnet Fe$_3$Sn$_2$. *J. Phys. Condens. Matter* **21,** 452202 (2009).
34. Raquet, B., Viret, M., Sondergard, E., Cespedes, O. & Mamy, R. Electron-magnon scattering and magnetic resistivity in 3d ferromagnets. *Phys. Rev. B* **66,** 024433 (2002).
35. Richard, P. et al. Observation of Dirac cone electronic dispersion in BaFe$_2$As$_2$. *Phys. Rev. Lett.* **104,** 137001 (2010).
36. Tan, S. Y. et al. Observation of Dirac cone band dispersions in FeSe thin films by photoemission spectroscopy. *Phys. Rev. B* **93,** 104513 (2016).
37. Bostwick, A., Ohta, T., Seyller, T., Horn, K. & Rotenberg, E. Quasiparticle dynamics in graphene. *Nat. Phys.* **3,** 36–40 (2007).
38. Nevius, M. S. et al. Semiconducting graphene from highly ordered substrate interactions. *Phys. Rev. Lett.* **115,** 136802 (2015).
39. Damascelli, A., Hussain, Z. & Shen, Z.-X. Angle-resolved photoemission studies of the cuprate superconductors. *Rev. Mod. Phys.* **75,** 473–541 (2003).
40. Onose, Y. et al. Observation of the magnon Hall effect. *Science* **329,** 297–299 (2010).
41. Chisnell, R. et al. Topological magnon bands in a kagome lattice ferromagnet. *Phys. Rev. Lett.* **115,** 147201 (2015).
42. Inami, T., Nishiyama, M., Maegawa, S. & Oka, Y. Magnetic structure of the kagome lattice antiferromagnet potassium jarosite KFe$_3$(OH)$_6$(SO$_4$)$_2$. *Phys. Rev. B* **61,** 12181–12186 (2000).
43. Hiroi, Z. et al. Spin-1/2 kagome-like lattice in volborthite Cu$_3$V$_2$O$_7$(OH)$_2 \cdot$ 2H$_2$O. *J. Phys. Soc. Jpn* **70,** 3377–3384 (2001).
44. Qi, X. L., Wu, Y.-S. & Zhang, S.-C. Topological quantization of the spin Hall effect in two-dimensional paramagnetic semiconductors. *Phys. Rev. B* **74,** 085308 (2006).
45. Sinitsyn, N. A., MacDonald, A. H., Jungwirth, T., Dugaev, V. K. & Sinova, J. Anomalous Hall effect in a two-dimensional Dirac band: the link between the Kubo-Streda formula and the semiclassical Boltzmann equation approach. *Phys. Rev. B* **75,** 045315 (2007).
46. Haldane, F. D. M. Berry curvature on the Fermi surface: anomalous Hall effect as a topological Fermi-liquid property. *Phys. Rev. Lett.* **93,** 206602 (2004).
47. Fang, Z. et al. The anomalous Hall effect and magnetic monopoles in momentum space. *Science* **302,** 92–95 (2003).
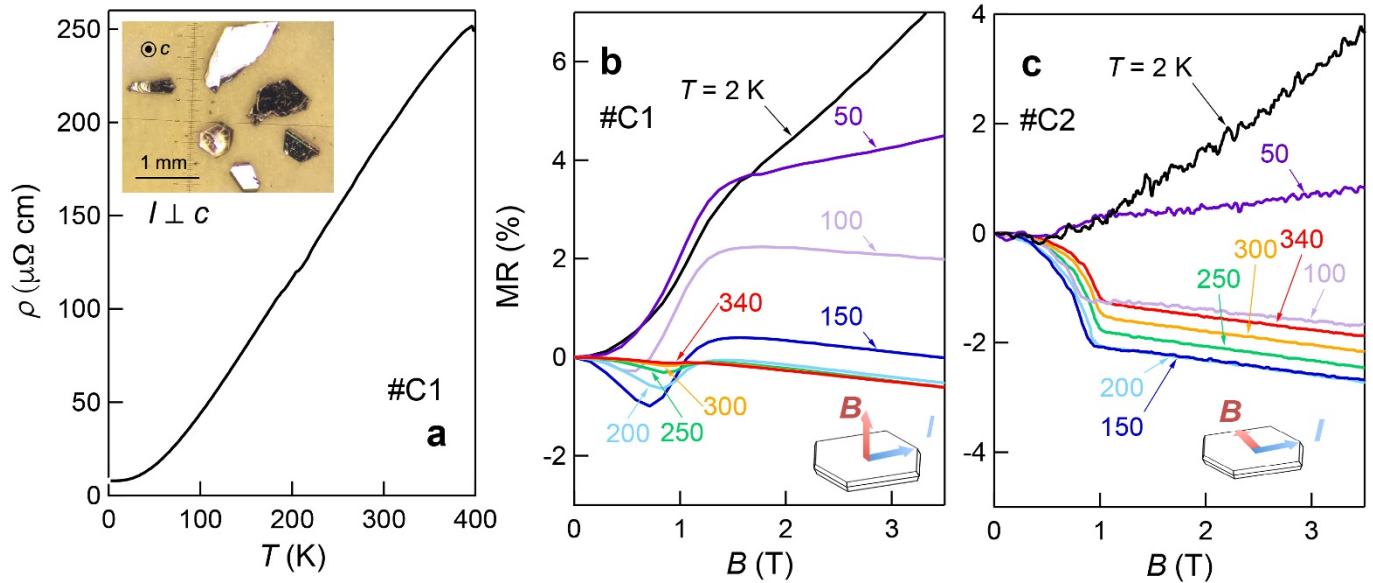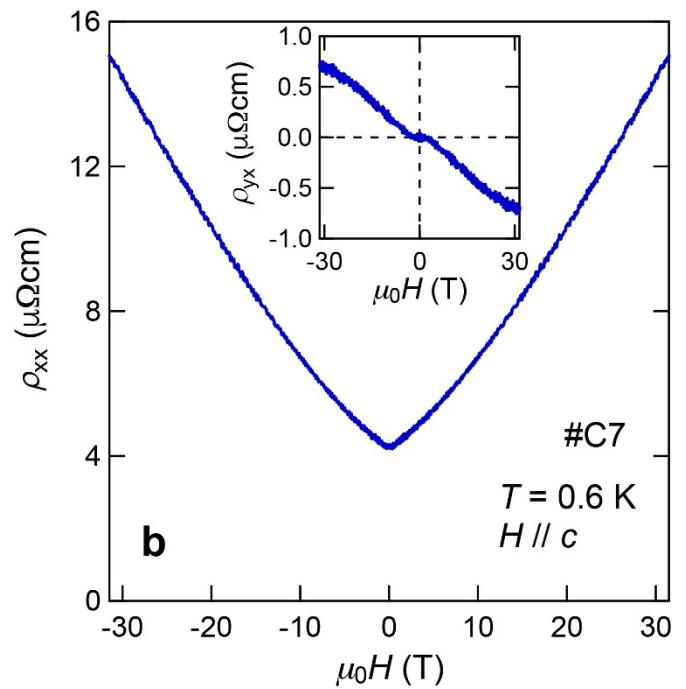
Extended Data Figure 1 | Metallic transport in Fe₃Sn₂. a, Resistivity ρ as a function of temperature T in the kagome plane for Fe_3Sn_2 sample C1. The inset shows a photograph of Fe_3Sn_2 single crystals.

b, c, Magnetoresistance (defined as $MR = [\rho_{xx}(B) - \rho_{xx}(0)]/\rho_{xx}(0)$) at selected T with B applied perpendicular (**b**) or parallel (**c**) to the kagome plane and $B \perp I$ (schematics of the configurations are shown as insets).
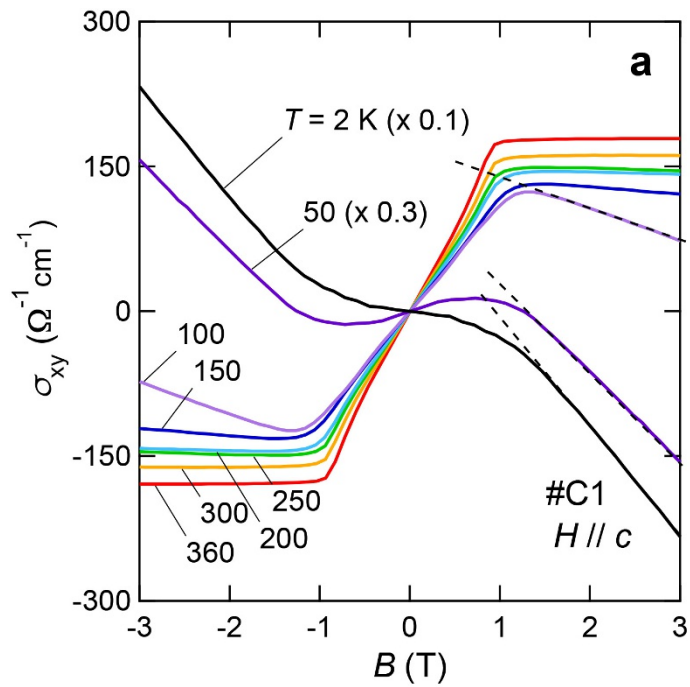
Extended Data Figure 2 | Extracting anomalous Hall conductivity and high-field transport. a, In-plane Hall conductivity σ_{xy} as a function of magnetic induction B at selected temperatures. Dashed lines represent the linear fit to σ_{xy}^{N}. The data at 2 K and 50 K have been scaled by the factors shown for clarity. **b**, Magnetoresistance (main panel) and Hall effect (inset) of Fe_3Sn_2 with applied magnetic field $\mu_0H \parallel c$ up to 31 T.
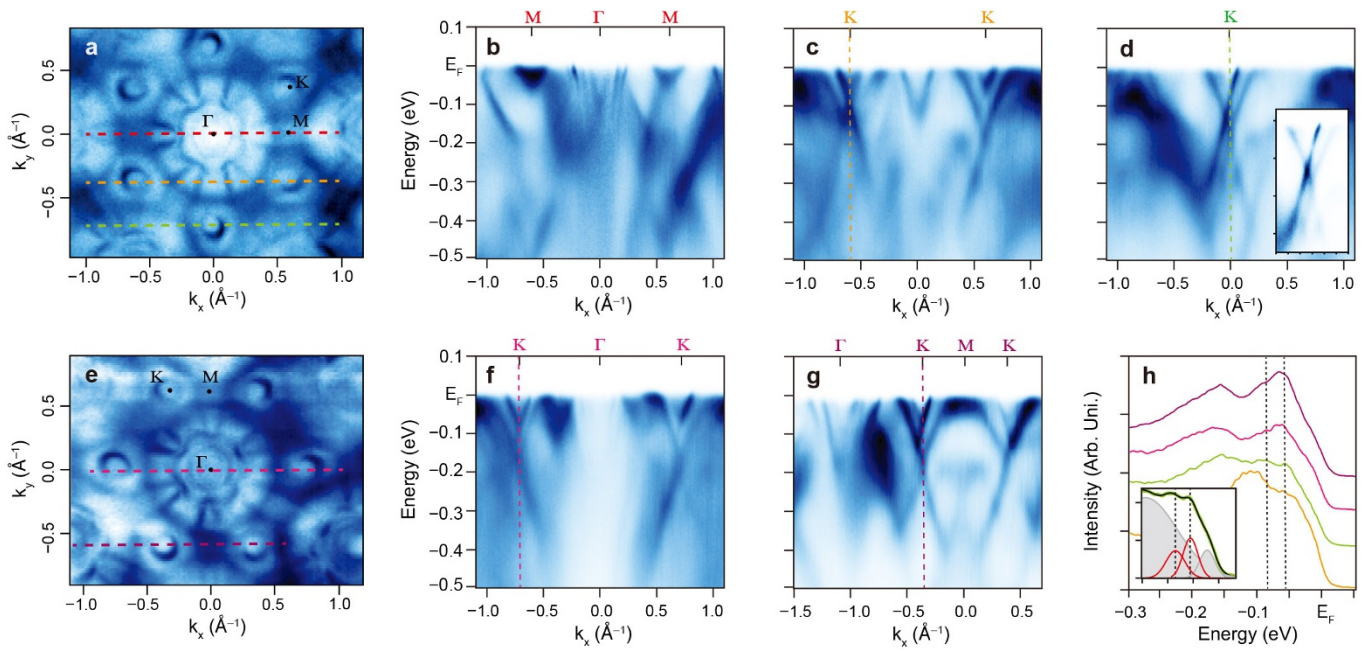
Extended Data Figure 3 | Momentum and energy-dependent band structure along high-symmetry directions. a, e, Fermi surface of Fe_3Sn_2 obtained from different experimental geometries. **b–d, f, g,** Band dispersion of Fe_3Sn_2 along high-symmetry directions. The panels correspond to the momentum directions along the red (**b**), orange (**c**), green (**d**), magenta (**f**) and purple (**g**) dotted lines in **a** and **e**. The inset in **d** shows the raw data of Fig. 3c (with the same energy and momentum range), highlighting the spectral weight distribution near the Dirac points. **h,** Energy distribution curves at different K points indicated in **c, d, f** and **g**. The curves are shifted along the vertical direction for clarity. The inset shows an example of Gaussian fits; the extracted gap size is $\Delta = 30 \pm 5$ meV.
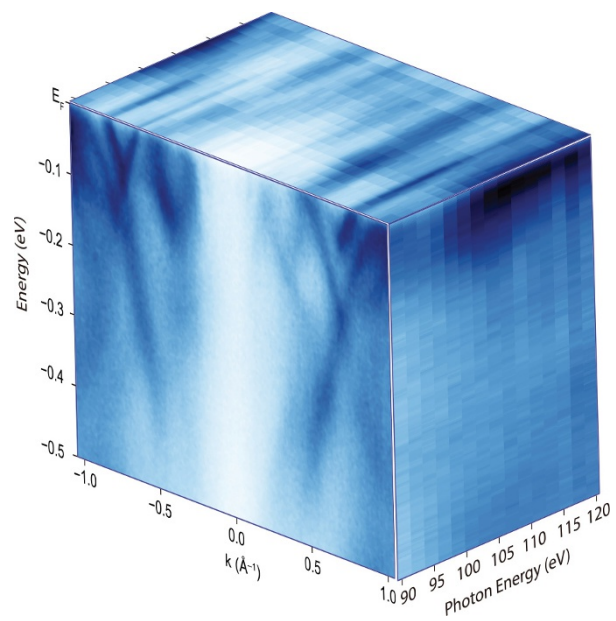
Extended Data Figure 4 | Photon-energy dependence of ARPES spectra.
ARPES intensity plot for Fe_3Sn_2 taken along the Γ–K direction as a
function of binding energy k and photon energy.
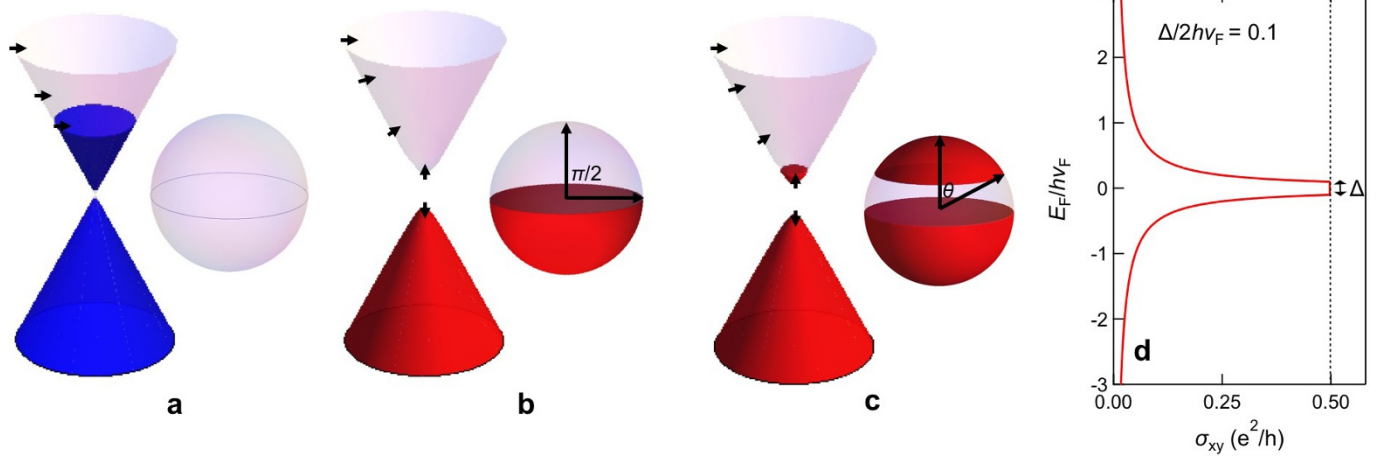
Extended Data Figure 5 | Berry curvature and Hall conductivity for a massive Dirac fermion. a–c, Schematics of 2D Dirac fermions and the corresponding Bloch-sphere representation of the wavefunction of filled states for the gapless case (**a**) and the gapped case with E_F in (**b**) and out of (**c**) the gap. **d**, Fermi energy E_F dependence of σ_{xy} for the case of a single massive Dirac fermion with gap Δ and Fermi velocity v_F.